#### **Research Article**

Anwar Ali Aldhafeeri\*

# Analyzing the 3D-MHD flow of a sodium alginatebased nanofluid flow containing alumina nanoparticles over a bi-directional extending sheet using variable porous medium and slip conditions

https://doi.org/10.1515/ntrev-2024-0077 received April 25, 2024; accepted July 14, 2024

Abstract: The sodium alginate (SA)-based nanofluid flow comprising alumina nanoparticles on a bi-directional extending sheet has many applications, which include thermal management, automotive radiators, industrial heat exchangers, conductive coatings, flexible electronics, electromagnetic shielding, solar panels, etc. A numerical study based on the SA-based nanofluid flow containing alumina nanoparticles over a bidir po foc na OV me de hea ha as or cal OD Fro ind tra tio rat the tri na

when matched to the slip condition. It is concluded from the observed results that the percentage increase is higher for the no-slip conditions compared to the slip conditions.

Keywords: nanofluids, non-Newtonian fluid, MHD, variable porous medium, thermal radiation, heat source, slip conditions

Stefan-Boltzmann constant

#### Nomenclature

irectional extending sheet in the presence of variable Darcy	Nome	iciature
orous media has not yet been examined. Therefore, this study ocuses on numerically investigating the flow behavior of a anofluid of SA containing nanoparticles of alumina (Al <sub>2</sub> O <sub>3</sub> ) wer a bi-directional extending sheet. The variable Darcy porous nedia, magnetic field, thermal radiation, and thermal-dependent and space-dependent heat sources are applied to examine eat transfer flow. The velocity and thermal slip conditions ave been used in the present model. The model is first shown is partial differential equations (ODEs). A numerical technique alled byp4c MATLAB function is applied to solve the modeled oDEs. The model is validated with previously published results. From the obtained results, it is found that high magnetic factor increases the thermal distribution, skin frictions, and heat transfer rate and reduces the velocity profiles along both directors. The Casson factor reduces the skin friction, heat transfer ate, and velocity profiles along both directions while increasing the thermal distribution. High velocities and temperature distributions of a SA-based nanofluid flow containing alumina anoparticles are found for the scenario of no-slip condition	$A^*, B^*, C^*$ $b, c$ $B_0$ $C_p$ $D_a$ $m$ $M$ $k$ $k^*$ $Pr$ $P_y$ $q_1, q_2$ $Q_{Td}, Q_{Sd}$ $Rd$ $\Re_0$ $u, v, w$ $u_w, v_w$ $v_f$ $x, y, z$	slips coefficients stretching constants strength of magnetic field specific heat Darcy parameter particle diameter magnetic factor thermal conductivity mean absorption coefficient Prandtl number fluid yield stress thermal and space-dependent heat source coefficients thermal and space-dependent heat source coefficients thermal and space-dependent heat source sefficients thermal and space-dependent service stretching flow in x- and y-directions kinematic viscosity coordinates
Corresponding author: Anwar Ali Aldhafeeri, Department of lathematics and Statistics, Faculty of Science, King Faisal University, O. Box 400, Al-Ahsa, 31982, Saudi Arabia,	μ ρ σ	dynamic viscosity density electrical conductivity

Ma e-mail: aaaldhafeeri@kfu.edu.sa

 $\sigma^*$ 

2 — Anwar Ali Aldhafeeri DE GRUYTER

,	volume fraction of the solid nanoparticle
$\beta_1$	ratio factor
γ	velocity slip factor along primary direction
,	velocity slip factor along the secondary
	direction
S	thermal slip factor
3	Casson factor

#### Base fluid

SA sodium alginate

## Nanoparticle

Al<sub>2</sub>O<sub>3</sub> alumina

### **Subscripts**

F base fluid nf nanofluid S nanoparticle

### 1 Introduction

Nanofluid flow, a burgeoning field in fluid dynamics and heat transfer, involves the mixing of nanoparticles in a pure fluid, offering remarkable enhancements in thermal conductivity as observed by Choi and Eastman [1]. This innovation has spurred extensive research due to its potential applications in numerous industries, including coolant of electric devices, and biomedical devices [2]. The unique characteristics of nanofluids, such as Brownian motion and increased surface area, lead to enhanced convective heat transfer coefficients and reduced width of the thermal layer at the boundary, thus significantly augmenting heat transfer rates compared to conventional fluids [3]. The impacts of nanofluid flow on thermal flow are intense, with notable improvements in heat dissipation and thermal management efficiency, ultimately leading to enhanced system performance and reliability [4]. It has been proved by Acharya et al. [5] that the existence of a nano-layer has augmented the thermal flow panels by 84.6% in comparison to the nanoparticles' diameter; however, challenges remain in understanding the complex relationship between nanoparticle dispersion, fluid

flow dynamics, and heat transfer mechanisms, as well as in optimizing nanofluid properties for specific applications while addressing concerns related to stability, sedimentation, and potential nanotoxicity. Despite these challenges, ongoing research endeavors continue to progress the nanofluid performance and its implications for heat transfer processes, paving the way for the development of novel thermal management solutions with enhanced efficiency and sustainability. Gherieb et al. [6] examined the dynamics of radiative and slip effects on Magnetohydrodynamics (MHD) nanofluid flow on a permeable surface and noticed that velocity distribution increased while thermal panels decreased with the increase in permeability factor and positive values of slip factor. Lone et al. [7] discussed the creation of entropy for nanofluid flow on a Riga sheet with nonlinearly convective effects. Asghar et al. [8] discussed mixed convective 2D radiative nanofluid flow on an exponentially shrinking surface with slip constraints and observed that thermal distribution has augmented in the second solution for the upsurge in the mixed convective factor while no variations have occurred in the first solution for the same phenomenon. Bhatti et al. [9] studied nanofluid flow on an elastic flat plate and applied this concept to solar energy systems. Asghar et al. [10] discussed the impacts of thermal radiations on 3D gyrating magnetized nanofluid flow and noticed that with the increase in magnetic factor and concentration of nanoparticles, there has been an increase in thermal profiles. Asghar et al. [11] inspected double solutions for convectively gyrating hybrid nanofluid flow on a linear contracting as well as elongating surface. Wagas et al. [12] noticed an augmentation in the heat transference phenomenon for nanofluid flow on an elongating sheet. Al-Kouz et al. [13] studied the thermal performance for radiative MHD tri-hybrid nanofluid flow on a vertical cylinder and noticed that the thermal characteristics increased augmented with the increase in the magnetic factor and nanoparticles' concentration.

Non-Newtonian fluids, display viscosity that deviates with the applied stress or shear rate. This diverse category encompasses a wide range of materials, including shearthinning fluids [14] (e.g., polymer solutions), shear-thickening fluids [15] (e.g., cornstarch in water), and viscoelastic fluids [16] (e.g., certain types of gels). In heat transfer processes, the rheological behavior of these fluids profoundly influences convective heat transfer rates and thermal boundary layer characteristics [17]. For instance, shear-thinning fluids display lessening viscosity for increasing shear rate, resulting in reduced flow resistance and enhanced heat transfer coefficients compared to Newtonian fluids [18]. Conversely, shear-thickening fluids experience viscosity increases under higher shear rates, leading to intensified flow resistance and altered

convective heat transfer patterns. Viscoelastic fluids, characterized by both viscous and elastic properties, often exhibit complex flow phenomena such as vortex shedding and flow instabilities, significantly impacting heat transfer efficiency and heat distribution within the system. The rheological properties and flow performance of these fluids (non-Newtonian) are vital for optimizing thermal flow processes in various applications, including food processing, oil recovery, and biomedical engineering, where these fluids are frequently encountered [19]. Despite the challenges posed by their intricate behavior, advancements in computational modeling techniques and experimental methodologies continue to deepen our understanding of non-Newtonian fluid flow and its intricate interplay with heat transfer phenomena, fostering the development of more efficient and tailored heat transfer solutions for diverse industrial and technological applications. Nazeer et al. [20] analyzed numerically non-Newtonian multiphase fluid flow on an inclined conduit and noticed that flow has weakened with expansion in Hartman number. Biswal et al. [21] inspected magnetized radiative non-Newtonian fluid flow on the nonlinearly elongated surface using Dufour and Soret impacts.

MHD is a multidisciplinary field that discovers the behavior of electrically conducting fluids with the effects of magnetic fields, with significant implications for heat transfer processes [22]. In MHD, the interface of magnetic field and fluid motion leads to complex phenomena that profoundly influence heat transfer characteristics [23]. One of the primary effects is MHD convection, where a magnetic field alters the fluid flow patterns and heat transfer rates. This occurs due to the Lorentz force, which induces electric currents in the conducting fluid when subjected to both a temperature gradient and a magnetic field. These induced currents interact with the magnetic field and the fluid motion, modifying the heat transfer process. In some cases, MHD enhances heat transfer by promoting more efficient fluid mixing and convective heat transport [24]. However, MHD can also suppress turbulence, which may reduce heat transfer rates, particularly in scenarios involving turbulent flows. Additionally, MHD can be employed to reduce drag in conducting fluid systems, such as liquid metal cooling systems, thereby minimizing frictional losses and enhancing heat transfer efficiency [25]. Furthermore, MHD principles find application in the areas, where careful control of magnetic fields can improve heat transfer performance. In MHD power generation systems, which convert heat energy from high-temperature fluids such as plasma or molten metals into electrical energy, understanding and manipulating MHD effects are crucial for maximizing energy conversion efficiency [26]. The study of MHD and its impacts on thermal flow plays a vigorous role in various industrial,

environmental, and engineering applications, shaping the design and optimization of systems involving conducting fluids and magnetic fields [27]. Tarakaramu et al. [28] studied MHD fluid flow with convective constraints and nonlinearly radiative effects along with thermal absorption. Mirzaei et al. [29] examined convective thermal transmission for MHD fluid flow in a circular channel using numerous constraints. Ayub et al. [30] scrutinized nanoscale thermal transference for trihybrid nanofluid flow on a gyrating heated surface. Botmart et al. [31] studied infinite share rate for nanofluid on a channel in cylindrical shape with effects of inclined magnetic field and activation energy. Lund et al. [32] discussed Casson magnetized hybrid nanofluid flow on a permeable surface with Joule heating as well as thermally radiative effects and established two distinct solutions for velocity ratio factor in contrast to copper-nanoparticles concentration and Casson factor.

A porous surface is a material that encompasses consistent void spaces, typically on or near its outermost layer. A variable porous medium describes a material that exhibits spatially varying characteristics related to its porosity, permeability, and other relevant properties. Variable porous media, characterized by spatially varying porosity [33], and other relevant properties, exert profound influences on heat transfer processes across a wide range of natural and engineered systems [34]. These variations introduce complexities in fluid flow patterns, thermal conductivity, and heat generation rates, leading to heterogeneous heat transfer phenomena. Spatial variability in porosity and permeability induces variations in convective heat transfer coefficients, promoting enhanced heat exchange in regions with higher fluid flow rates while impeding heat transfer in regions with lower flow rates [35]. Heterogeneous heat generation within the medium further complicates temperature distributions, influencing overall heat transfer rates. Thermal conductivity variations, stemming from changes in porosity and solid phase properties, introduce spatially dependent thermal resistance, affecting heat conduction within the medium [36]. Additionally, nonlinear thermal behavior may arise from phenomena such as thermal expansion or phase change, further influencing heat transfer processes. Understanding and analyzing these complex interactions require advanced mathematical modeling and numerical simulation techniques to accurately predict temperature distributions and optimize heat transfer efficiency in variable porous media systems. Reddy et al. [37] debated on thermal flow phenomenon for fluid flow on a permeable medium along an elongating cylinder. Hussain and Sheremet [38] examined convective and radiative fluid flow through a penetrable sheet with impacts of inclined magnetic effects. Khan et al. [39] discussed fluid flow on a porous sheet and noticed that with intensification in permeability effects, there is intensification in thermal flow panels. Gorai *et al.* [40] studied the time-dependent nanofluid flow on a medium with varying characteristics in the porosity of the surface.

Thermal radiation is an electromagnetic radiation emitted by the surfaces of objects due to their temperature. Thermal radiation exerts significant impacts on heat transfer processes in fluid flow scenarios on surfaces [41]. When a fluid moves on a surface, such as air over a heated object or water over a hot plate, thermal radiation backs the exchange of heat amid the fluid and sheet [42]. This radiation is emitted by the surface according to its temperature and emissivity and can be absorbed or scattered by the fluid. As the fluid engrosses radiations, its temperature increases, altering its density, viscosity, and thermal conductivity, thereby affecting fluid flow patterns and heat transfer characteristics [43]. Thermal radiation can influence boundary layer development, particularly in scenarios with high-temperature differentials, where radiative heating of the fluid near the surface can accelerate boundary layer growth and transition to turbulent flow [44]. Conversely, in cases where the fluid is optically thick and absorbs a significant portion of incident radiation, the temperature gradient near the surface may decrease, leading to reduced thermal boundary layer thickness and convective heat transfer rates. Furthermore, thermal radiation can interact with convective heat transfer mechanisms, such as forced convection from bulk fluid motion or natural convection due to buoyancy effects, altering temperature distributions and heat transfer coefficients along the surface. The relationship between thermal radiation and fluid flow is crucial for optimizing heat transfer processes in numerous applications in the field of engineering, including thermal management systems, and aerospace propulsion systems, where efficient heat transfer is essential for performance, safety, and reliability [45,46]. Guedri et al. [47] analyzed mathematically the thermally radiated fluid flow on a contracting surface with unsteady effects. Farooq et al. [48] studied the thermally radiated effects on nanofluid flowing on an elongating sheet and have solved the governing equation using a non-similar approach. Darvesh et al. [49] examined the rate of infinite share for the model of viscosity regarding cross-flow of fluid with impacts of nanoparticles and gyrotatic microorganisms on a 3D cylinder and have observed that with small changes in Brownian factor and nanoparticles' concentration, there has been a reduction of 78.44% in microorganisms' concentration. Asghar et al. [50] studied mixed convective 2D MHD nanofluid flow on an exponentially contracting surface with impacts of thermal and flow slip constraints.

Based on the above survey, it is certain that the numerical study of a sodium alginate (SA)-based nanofluid flow

containing alumina nanoparticles over a bi-directional extending sheet in the presence of variable Darcy porous media has not been discussed. Therefore, in the present analysis, we have presented the numerical analysis of a nanofluid flow on a bi-directional extending sheet has been presented. The Casson model is incorporated to investigate the SA-based nanofluid flow containing alumina nanoparticles. The variable Darcy porous media, magnetic field, thermal radiation, and thermal-dependent and space-dependent heat sources are applied to examine heat transfer flow. The velocity and thermal slip conditions are used in this study.

## 2 Problem formulation

Assume the SA-based nanofluid flow comprising nanoparticles of Al<sub>2</sub>O<sub>3</sub> on a bi-directional extending sheet. The Cartesian coordinate system (x, y, z) is taken such that the flow components (u, v, w) are chosen in x-, y-, and z-directions. The stretching velocities in x- and y-directions are  $u_w = bx$  and  $v_w = cy$  with b and c are fixed values. A magnetic field with strength  $B_0$  is used along the z-axis which is perpendicular to the x- and y-axes as shown in Figure 1. Velocity and thermal slip conditions are applied to control the flow characteristics and enhance the thermal transfer by reducing the thermal performance at the boundary in various engineering applications. Furthermore, thermal radiation, thermal-dependent, and spacedependent heat sources are applied to investigate heat transfer flow. In the present analysis, the viscous dissipation, Joule heating, heat source, stretching/shrinking, and thermal and mass flux conditions are not taken into consideration. Following previous literature [33,51–53], the variable Darcy model is defined as:

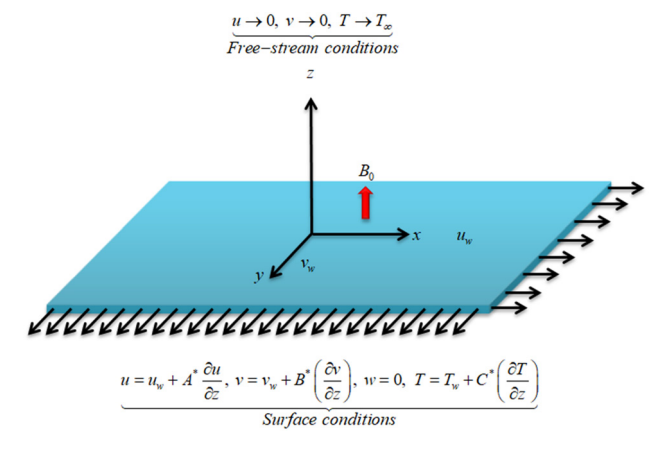


Figure 1: Geometrical representation of the flow problem.

$$K(z) = \frac{m^2 \Re(z)^3}{(1 - \Re(z))^2} \quad \text{where } \Re(z) = \Re_0 \left[ 1 + \Re_1 e^{\frac{x \Re_2}{m}} \right], \quad (1)$$

where  $\Re_1$  and  $\Re_2$  are fixed (empirical) values, m is the diameter of the particle, and  $\mathfrak{R}_0$  is the ambient porosity. It should be noted that  $\mathfrak{R}_0$ ,  $\mathfrak{R}_1$ , and  $\mathfrak{R}_2$  are chosen to be fixed during numerical simulation.

The non-Newtonian Casson model is incorporated in such a way that the nanofluid flow exhibits the non-Newtonian behavior. The rheological model for Casson nanofluid flow is defined as [54]:

$$\tau_{ij} = \begin{cases} 2e_{ij} \left[ \mu + \frac{P_{y}}{\sqrt{2\pi}} \right] & \text{when } \pi > \pi_{c} \\ 2e_{ij} \left[ \mu + \frac{P_{y}}{\sqrt{2\pi_{c}}} \right] & \text{when } \pi_{c} > \pi, \end{cases}$$
 (2)

where  $P_v$  is the fluid yield stress, which is defined as  $P_{y} = \frac{\mu\sqrt{2\pi}}{B}$ .

This expression is reduced to

$$\mu_{\rm b} = \frac{\mu}{\rho} \left[ 1 + \frac{1}{\beta} \right]. \tag{3}$$

Using the above assumptions, we have [55,56]

$$\frac{\partial u}{\partial x} + \frac{\partial v}{\partial y} + \frac{\partial w}{\partial z} = 0,$$
 (4)

$$\rho_{\rm nf} \left[ u \frac{\partial u}{\partial x} + v \frac{\partial u}{\partial y} + w \frac{\partial u}{\partial z} \right]$$

$$= \mu_{\rm nf} \left[ 1 + \frac{1}{\beta} \frac{\partial^2 u}{\partial z^2} - \sigma_{\rm nf} B_0^2 u + \frac{\mu_{\rm nf}}{K(z)} u, \right]$$
(5)

$$\rho_{\rm nf} \left[ u \frac{\partial v}{\partial x} + v \frac{\partial v}{\partial y} + w \frac{\partial v}{\partial z} \right]$$

$$= \mu_{\rm nf} \left[ 1 + \frac{1}{\beta} \frac{\partial^2 v}{\partial z^2} - \sigma_{\rm nf} B_0^2 v + \frac{\mu_{\rm nf}}{K(z)} v, \right]$$
(6)

$$(\rho C_{\rm p})_{\rm nf} \left[ u \frac{\partial T}{\partial x} + v \frac{\partial T}{\partial y} + w \frac{\partial T}{\partial z} \right]$$

$$= k_{\rm nf} \frac{\partial^2 T}{\partial z^2} + \frac{16\sigma^* T_{\infty}^3}{3k^*} \frac{\partial^2 T}{\partial z^2} + q_1(T - T_{\infty}) + q_2(T_{\rm w} - T_{\infty}) \exp(-a\eta).$$
(7)

The constraints at the boundary are

$$u = u_{W} + A^{*} \frac{\partial u}{\partial z}, \quad v = v_{W} + B^{*} \left(\frac{\partial v}{\partial z}\right), \quad w = 0,$$

$$T = T_{W} + C^{*} \left(\frac{\partial T}{\partial z}\right) \text{ at } z = 0,$$

$$u \to , \quad v \to 0, \quad T \to T_{\infty} \text{ as } z \to \infty.$$

(8)

Table 1: Thermophysical relations for the nanofluid [57,58]

Property	Thermophysical relation
Dynamic viscosity	$\frac{\mu_{\rm nf}}{\mu_{\rm f}} = \frac{1}{(1-\zeta)^{2.5}}$
Density	$\frac{\rho_{\rm nf}}{\rho_{\rm f}} = (1 - \zeta) + \zeta \frac{\rho_{\rm s}}{\rho_{\rm f}}$
Heat capacitance	$\frac{(\rho C_{\rm p})_{\rm nf}}{(\rho C_{\rm p})_{\rm f}} = (1 - \zeta) + \zeta \frac{(\rho C_{\rm p})_{\rm s}}{(\rho C_{\rm p})_{\rm f}}$
Electrical conductivity	$\frac{\sigma_{\rm nf}}{\sigma_{\rm f}} = 1 + \frac{3\left(\frac{\sigma_{\rm S}}{\sigma_{\rm f}} - 1\right)\zeta}{\left(\frac{\sigma_{\rm S}}{\sigma_{\rm f}} + 2\right) - \left(\frac{\sigma_{\rm S}}{\sigma_{\rm f}} - 1\right)\zeta}$
Thermal conductivity	$\frac{k_{\text{nf}}}{k_{\text{f}}} = \frac{(k_{\text{S}} + 2k_{\text{f}}) - 2(k_{\text{f}} - k_{\text{S}})\zeta}{(k_{\text{S}} + 2k_{\text{f}}) + (k_{\text{f}} - k_{\text{S}})\zeta}$

The thermophysical relations are described in Table 1. The experimental values of the base fluid as well as nanoparticles are defined in Table 2.

The similarity variables are demarcated as [55,59]

$$\xi = z \sqrt{\frac{c}{v_{\rm f}}}, \quad u = cx(f'(\xi)), \quad v = cyg'(\xi),$$

$$T = T_{\infty} + (T_{\rm w} - T_{\infty})\theta(\xi), \quad w = -\sqrt{cv_{\rm f}}(f(\xi) + g(\xi)).$$
(9)

Using (9), the leading equations are transformed as

$$\left(1 + \frac{1}{\beta}\right) f''' - A_1 A_2 \{f'^2 - (f + g)f''\} - \left[A_1 A_3 M - \frac{1}{D_a} \frac{\left[1 - \Re_0 \left(1 + \Re_1 e^{\frac{-\Re_2 \xi}{\sqrt{D_a}}}\right)\right]^2}{\left[\Re_0^3 \left(1 + \Re_1 e^{\frac{-\Re_2 \xi}{\sqrt{D_a}}}\right)\right]^3}\right] f' = 0,$$
(10)

$$\left(1 + \frac{1}{\beta}\right)g''' - A_1 A_2 \{g'^2 - (g+f)g''\} - \left[A_1 A_3 M - \frac{1}{D_a} \left[\frac{1 - \varepsilon_0 \left[1 + \Re_1 e^{\frac{-\Re_2 \xi}{\sqrt{D_a}}}\right]^2}{\left[\Re_0^3 \left[1 + \Re_1 e^{\frac{-\Re_2 \xi}{\sqrt{D_a}}}\right]\right]^3}\right]g' = 0,$$
(11)

Table 2: Experimental values of base fluid and nanoparticles [57]

Property	SA	Alumina nanoparticle
ρ	989	3,970
$C_{ m p}$	4,175	765
k	0.6376	40
σ	$2.60 \times 10^{-4}$	$1.0 \times 10^{-10}$

$$(A_4 + \text{Rd})\theta'' + \text{Pr}\{A_5(f + g)\theta' + Q_{\text{Td}}\theta + Q_{\text{Sd}}\exp(-a\xi)\}\$$
  
= 0,

With subjected conditions at boundaries

$$f(0) = 0, f'(0) = 1 + f''(0)\alpha,$$

$$g'(0) = \beta_1 + g''(0)\gamma,$$

$$g(0) = 0, \theta(0) = 1 + \theta'(0)\delta,$$

$$g'(\infty) = 0, f'(\infty) = 0, \theta(\infty) = 0.$$
(13)

The dimensionless emerging factors are defined as follows with their physical description in the nomenclature table:

$$\begin{cases} A_{1} = \frac{\mu_{f}}{\mu_{nf}}, A_{2} = \frac{\rho_{nf}}{\rho_{f}}, A_{3} = \frac{\sigma_{nf}}{\sigma_{f}}, A_{4} = \frac{k_{nf}}{k_{f}}, \\ A_{5} = \frac{(\rho C_{p})_{nf}}{(\rho C_{p})_{f}}, \Pr = \frac{(\mu_{f} C_{p})_{f}}{k_{f}}, \quad Rd = \frac{16\sigma^{*}T_{\infty}^{3}}{3k^{*}k_{f}}, \quad \beta_{1} = \frac{b}{c}, \\ Q_{Td} = \frac{q_{1}}{c(\rho C_{p})_{f}}, \quad Q_{Sd} = \frac{q_{2}}{c(\rho C_{p})_{f}}, \quad \alpha = A^{*}\sqrt{\frac{c}{v_{f}}}, \\ D_{a} = \frac{v_{f}}{am^{2}}, \quad M = \frac{\sigma_{f}B_{0}^{2}}{c\rho_{f}}, \quad \gamma = B^{*}\sqrt{\frac{c}{v_{f}}}, \quad \delta = C^{*}\sqrt{\frac{c}{v_{f}}}. \end{cases}$$

$$(14)$$

#### **Interested quantities**

The skin frictions along *x*- and *y*-directions, and local Nusselt number are described as follows:

$$C_{\rm fx} = \frac{\tau_{\rm wx}}{\rho_{\rm f} u_{\rm w}^2}, \quad C_{\rm fy} = \frac{\tau_{\rm wy}}{\rho_{\rm f} u_{\rm w}^2}, \quad {\rm Nu}_{\rm x} = \frac{x q_{\rm w}}{k_{\rm f} (T_{\rm w} - T_{\infty})}, \quad (15)$$

where  $\tau_{\rm wx}$  and  $\tau_{\rm wy}$  are the shear stresses along the x- and y-directions, and  $q_{\rm w}$  is heat flux, mathematically these quantities are illustrated as:

(12) 
$$\tau_{\text{wx}} = \mu_{\text{nf}} \left[ 1 + \frac{1}{\beta} \left| \frac{\partial u}{\partial z} \right|_{z=0}, \quad \tau_{\text{wy}} = \mu_{\text{nf}} \left[ 1 + \frac{1}{\beta} \left| \frac{\partial v}{\partial z} \right|_{z=0}, \right]$$

$$q_{\text{w}} = -\left[ k_{\text{nf}} + \frac{16T_{\infty}^{3}\sigma^{*}}{3k^{*}} \left| \frac{\partial T}{\partial z} \right|_{z=0}.$$
(16)

Using similarity variables, equation (15) is reduced as follows:

$$C_{fx} = -C_{fx} Re_x^{1/2} = \frac{1}{A_1} \left( 1 + \frac{1}{\beta} \right) f''(0),$$

$$C_{fy} = -C_{fy} Re_y^{1/2} = \frac{1}{A_1} \left( 1 + \frac{1}{\beta} \right) g''(0),$$

$$Nu = Nu_x Re_x^{-1/2} = -(A_4 + Rd)\theta'(0).$$
(17)

## 3 Numerical solution

The approach called the bvp4c MATLAB function is chosen to solve the modeled equations numerically. This technique can solve the linear and nonlinear system of equations with minimal struggle, the system of equations that cannot be solved by analytical technique. This method can solve the modeled equations much faster than other methods. This method allows us to introduce our error tolerance. For the present, the error tolerance is chosen as  $10^{-6}$ . To introduce this method, we have to transform the higher-order system of equations to first-order system of equations. Therefore, we have defined the following relations.

$$f = \widehat{\delta}(1), \quad f'' = \widehat{\delta}(3), \quad f' = \widehat{\delta}(2), \quad f''' = \widehat{\delta}'(3),$$

$$g = \widehat{\delta}(4), \quad g'' = \widehat{\delta}(6), \quad g' = \widehat{\delta}(5), \quad g''' = \widehat{\delta}'(6), \quad (18)$$

$$\theta' = \widehat{\delta}(8), \quad \theta = \widehat{\delta}(7), \quad \theta'' = \widehat{\delta}'(8).$$

Using equation (18), equations (10)-(13) are transformed as

$$\widehat{\delta}'(3) = - \left\{ \frac{-A_1 A_2 \{ (\widehat{\delta}(2))^2 - (\widehat{\delta}(1) + \widehat{\delta}(4)) \widehat{\delta}(3) \} - \left[ A_1 A_3 M - \frac{1}{D_a} \frac{\left[ 1 - \mathfrak{R}_0 \left[ 1 + \mathfrak{R}_1 e^{\frac{-\mathfrak{R}_2 \mathcal{E}}{\sqrt{D_a}}} \right] \right]^2}{\left[ \mathfrak{R}_0^3 \left[ 1 + \mathfrak{R}_1 e^{\frac{-\mathfrak{R}_2 \mathcal{E}}{\sqrt{D_a}}} \right] \right]^3} \widehat{\delta}(2) \right\}}, \tag{19}$$

$$\widehat{\delta}'(6) = - \frac{\left[ -A_1 A_2 \{ (\widehat{\delta}(5))^2 - (\widehat{\delta}(1) + \widehat{\delta}(4)) \widehat{\delta}(6) \} - \left[ A_1 A_3 M - \frac{1}{D_a} \frac{\left[ 1 - \varepsilon_0 \left[ 1 + \mathfrak{R}_1 e^{\frac{-\mathfrak{R}_2 \xi}{\sqrt{D_a}}} \right]^2 \right]}{\left[ \mathfrak{R}_0^3 \left[ 1 + \mathfrak{R}_1 e^{\frac{-\mathfrak{R}_2 \xi}{\sqrt{D_a}}} \right] \right]^3} \widehat{\delta}(5)}{\left[ 1 + \frac{1}{\beta} \right]}, \tag{20}$$

**Table 3:** Comparison of the results of  $\theta'(0)$  for higher values of Pr when  $\zeta=0.0,\,\beta_1=0.0,\,\mathrm{Rd}=0.0,\,Q_{\mathrm{Td}}=0.0,\,Q_{\mathrm{Sd}}=0.0,\,\alpha=0.0,\,M=0.0,\,\gamma=0.0,\,\delta=0.0,\,\mathrm{and}\,\,\beta\to\infty$ 

Pr	0.07	0.2	0.7	2.0	7.0
Khan and Pop [60]	0.0663	0.1691	0.4539	0.9113	1.8954
Reddy Gorla and Sidawi [61]	0.0654	0.1691	0.5349	0.9114	1.8905
Al-Kouz and Owhaib [62]	0.06562	0.16909	0.45392	0.91136	1.89542
Dawar et al. [57]	0.0156648056	0.1690886199	0.4539174275	0.9113613928	1.8954202000
Present results	0.0156648110	0.1690884321	0.4539172074	0.9113612264	1.8954201100

$$\widehat{\delta}'(8) = -\left[\frac{\Pr\{A_{5}(\widehat{\delta}'(1) + \widehat{\delta}'(4))\widehat{\delta}'(8) + Q_{Td}\widehat{\delta}'(7) + Q_{Sd}\exp(-a\xi)\}}{(A_{4}+Rd)}\right]. \tag{21}$$

With subjected conditions at boundaries

$$\begin{split} \widehat{\delta_{a}}(1) &= 0, \quad \widehat{\delta_{a}}(2) - (1 + \alpha \widehat{\delta_{a}}(3)), \quad \widehat{\delta_{b}}(2) - 0, \\ \widehat{\delta_{a}}(4) &= 0, \quad \widehat{\delta_{a}}(5) - (\beta_{1} + \gamma \widehat{\delta_{a}}(6)), \quad \widehat{\delta_{b}}(5) - 0, \quad (22) \\ \widehat{\delta_{a}}(7) &= (1 + \delta \widehat{\delta_{a}}(8)), \quad \widehat{\delta_{b}}(7) - 0. \end{split}$$

In equation (22), the subscripts a and b show the initial and boundary conditions, respectively. Similarly, equation (17) is reduced as

$$C_{fx} = -C_{fx} Re_x^{1/2} = \frac{1}{A_1} \left[ 1 + \frac{1}{\beta} \right] \widehat{\delta} (3),$$

$$C_{fy} = -C_{fy} Re_y^{1/2} = \frac{1}{A_1} \left[ 1 + \frac{1}{\beta} \right] \widehat{\delta} (6),$$

$$Nu = Nu_x Re_x^{-1/2} = -(A_4 + Rd) \widehat{\delta} (8).$$
(23)

### 4 Validation

Table 3 depicts the comparative results of  $\theta'(0)$  for higher values of Pr when  $\zeta=0.0$ ,  $\beta_1=0.0$ , Rd = 0.0,  $Q_{\rm Td}=0.0$ ,  $Q_{\rm Sd}=0.0$ ,  $\alpha=0.0$ , M=0.0,  $\gamma=0.0$ ,  $\delta=0.0$ , and  $\beta\to\infty$ . This means that the present model is reduced to a classical Newtonian one where the magnetic field, variable Darcy model, slip conditions, and other external forces are ignored. From the obtained results, we have seen that the current results have a close relation with the available work of Khan and Pop [60], Reddy Gorla and Sidawi [61], Al-Kouz and Owhaib [62], and Dawar *et al.* [57].

## 5 Discussion of results

This paragraph deals with the obtained results in the present analysis of nanofluid flow on a bi-directional extending sheet and their physical discussion. The results are displayed in Tables 4 and 5 and Figures 2–15. The results are

**Table 4:** Effects of M,  $\beta$ , and  $\beta_1$  on  $C_{\rm fx}$  and  $C_{\rm fy}$ , when  $\alpha=0.0$ ,  $\alpha=0.5$ ,  $\gamma=0.0$ , and  $\gamma=0.5$ 

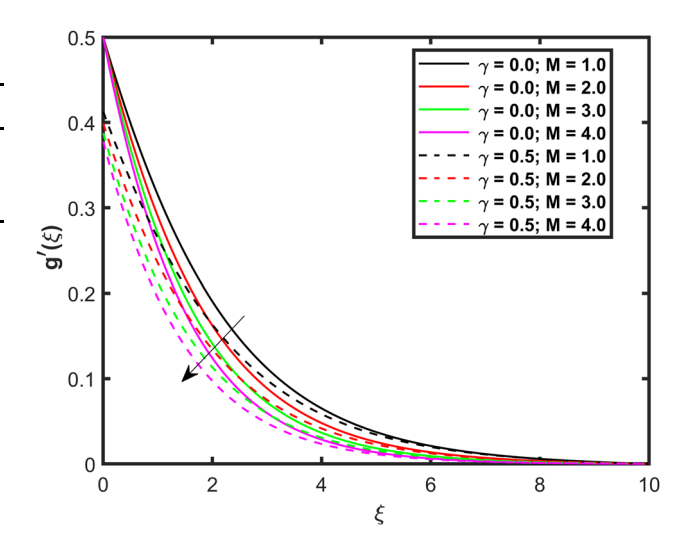
M	β	$oldsymbol{eta}_1$	$\mathcal{C}_{\mathrm{fx}}$			$oldsymbol{\mathcal{C}_{\mathrm{fy}}}$		
			$\alpha = 0.5$	<i>α</i> = 0.0	Percentage increase $\frac{(\alpha = 0.5) - (\alpha = 0.0)}{(\alpha = 0.5)}$	<i>γ</i> = 0.5	y = 0.0	Percentage increase $(y = 0.5) - (y = 0.0)$ $(y = 0.5)$
1.0			1.51211	2.46186	63	0.738401	1.150704	56
2.0			1.682701	2.872317	71	0.829569	1.367204	65
3.0			1.817558	3.23474	78	0.90035	1.556056	73
4.0			1.928548	3.562523	85	0.95796	1.725547	80
	1.0		1.309297	2.031519	55	0.626648	0.91909	47
	2.0		1.070322	1.744438	63	0.513991	0.787676	53
	3.0		0.984416	1.638964	66	0.473402	0.73944	56
	4.0		0.940037	1.583909	68	0.452413	0.714274	58
		1.0	1.356637	2.128421	57	1.356637	2.128421	57
		2.0	1.441038	2.308074	60	3.023132	5.234595	73
		3.0	1.515118	2.473702	63	4.881147	9.091776	86
		4.0	1.581318	2.628611	66	6.876749	13.58088	97

— Anwar Ali Aldhafeeri DE GRUYTER

**Table 5:** Effects of  $Q_{\rm Td}$ ,  $Q_{\rm Sd}$ ,  $\beta$ , and M on Nu, when  $\delta$  = 0.0 and  $\delta$  = 0.5

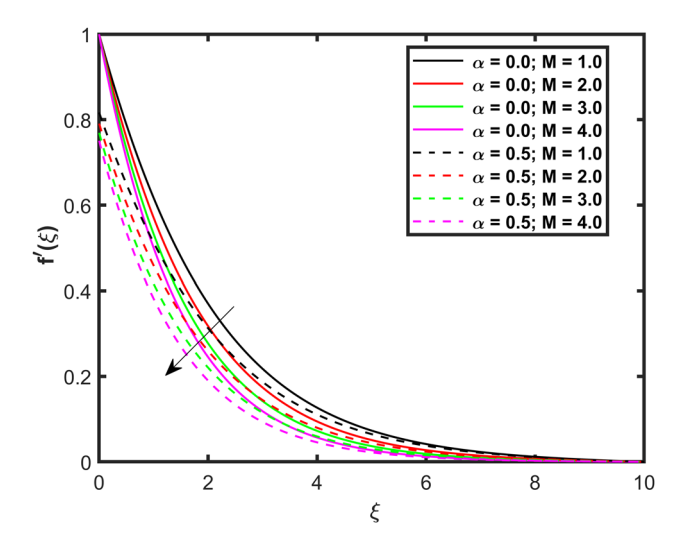
$Q_{\mathrm{Td}}$	$Q_{\rm Sd}$	β	M	Nu		
				δ = 0.5	δ = 0.0	Percentage increase $(\delta = 0.5)$ $(\delta = 0.0)$ $(\delta = 0.5)$
0.1				0.799088	1.368688	71
0.2				0.910912	1.638132	80
0.3				1.001175	1.880095	88
0.4				1.076019	2.100819	95
	0.10			0.178862	0.289978	62
	0.15			0.337814	0.547443	62
	0.20			0.496765	0.804754	62
	0.25			0.655722	1.062248	62
		1.0		0.655722	1.062248	62
		2.0		0.562694	0.889158	58
		3.0		0.512931	0.800884	56
		4.0		0.48159	0.74667	55
			0.1	0.611055	0.976764	60
			0.2	0.6261	1.005173	61
			0.3	0.640981	1.033697	61
			0.4	0.655722	1.062248	62

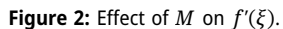
shown for both slip and no-slip constraints. The x-direction velocity factor is denoted by  $\alpha$ , y-direction velocity parameter is denoted by  $\gamma$ , and the temperature slip parameter is denoted by  $\delta$ . The slip conditions are applicable for the case when  $\alpha > 0$ ,  $\gamma > 0$ , and  $\delta > 0$ , while the no-slip conditions are applicable when  $\alpha = 0$ ,  $\gamma = 0$ , and  $\delta = 0$ . Table 4 portrays the effects of M,  $\beta$ , and  $\beta_1$  on  $C_{\rm fx}$  and  $C_{\rm fy}$ , when  $\alpha = 0.0$ ,  $\alpha = 0.5$ ,  $\gamma = 0.0$ , and  $\gamma = 0.5$ . From this Table, we observed that the higher magnetic factor (M), Casson factor ( $\beta$ ), and ratio factor ( $\beta_1$ ) increase  $C_{\rm fx}$  and  $C_{\rm fy}$ , whereas higher  $\beta$  reduces  $C_{\rm fx}$  and  $C_{\rm fy}$  for both slip ( $\alpha = 0.5$ ) and no-slip

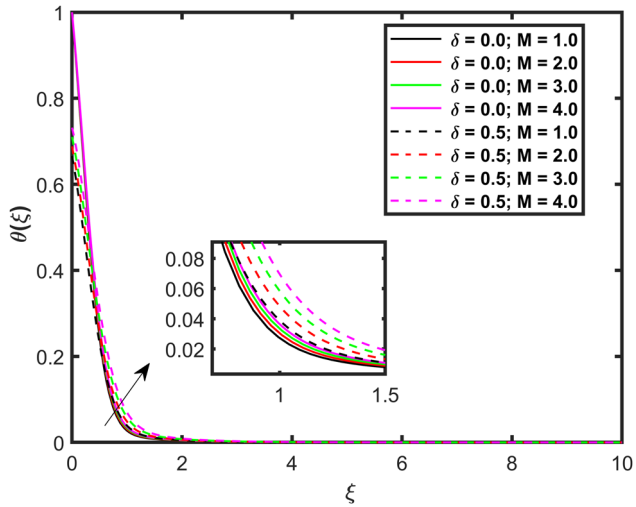


**Figure 3:** Effect of M on  $g'(\xi)$ .

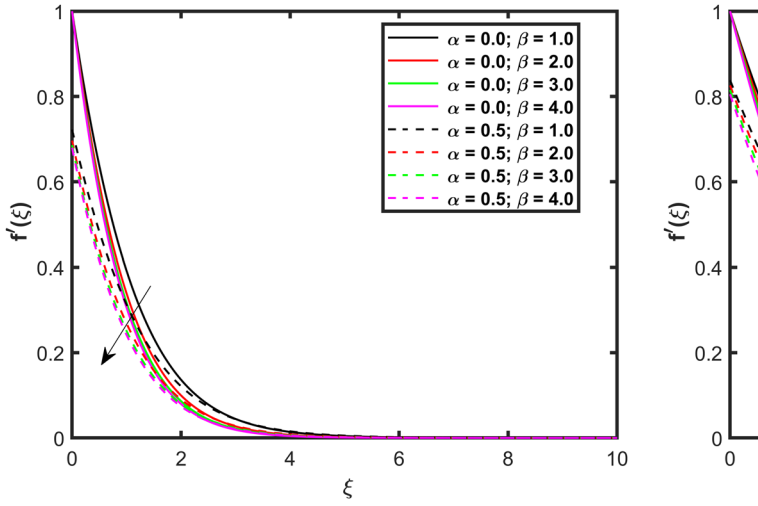
 $(\alpha=0.0)$  constraints. When M increases, the opposing force at the sheet's surface, also called friction force, increases. This means that higher values of M increases the friction force and results in higher  $C_{\rm fx}$  and  $C_{\rm fy}$  for the scenarios  $(\alpha=0.5)$  and  $(\alpha=0.0)$ . Table 5 shows the effects of  $Q_{\rm Td}$ ,  $Q_{\rm Sd}$ ,  $\beta$ , and M on Nu, when  $\delta=0.0$  and  $\delta=0.5$ . From this Table, we observed that the thermal-dependent heat source factor  $(Q_{\rm Td})$ , space-dependent heat source factor  $(Q_{\rm Td})$ , space-dependent heat source factor  $(\beta)$  reduces Nu for both slip  $(\delta=0.5)$  and no-slip  $(\delta=0.0)$  conditions. It is concluded from the observed results presented in Tables 4 and 5 that the percentage increase is higher for the no-slip conditions compared to the slip conditions. The details are presented in Figures 2–15. Figures 2–4 demonstrate the deviations in velocity  $(f'(\xi), g'(\xi))$  and

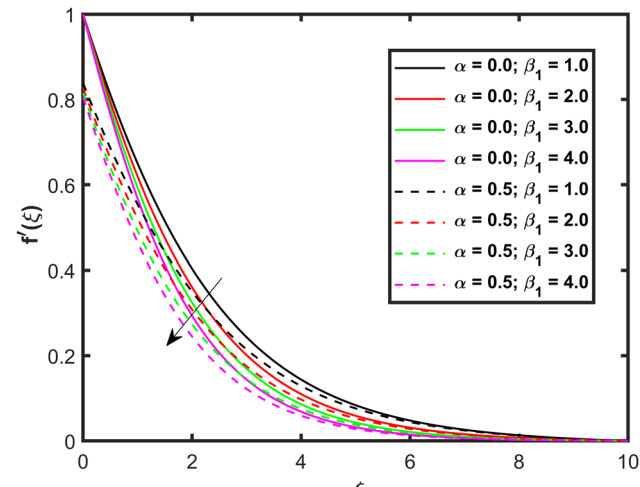






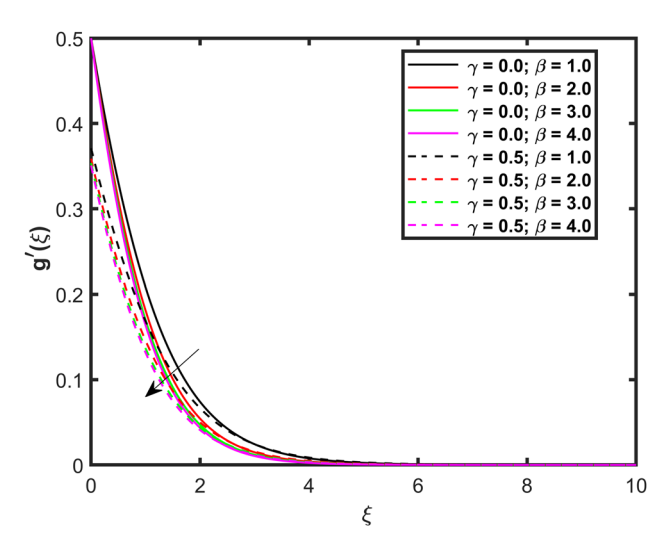
**Figure 4:** Effect of M on  $\theta(\xi)$ .

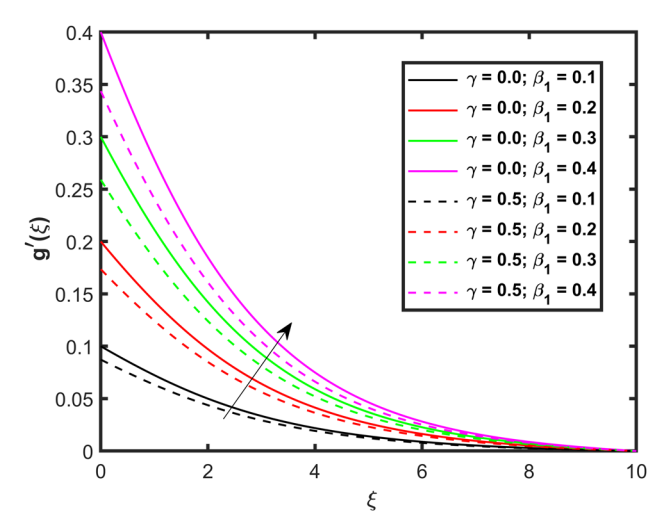




**Figure 5:** Effect of  $\beta$  on  $f'(\xi)$ .

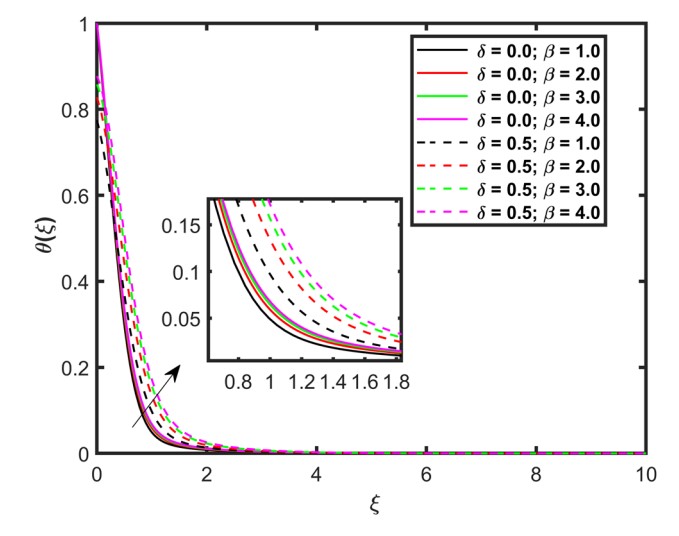
**Figure 8:** Effect of  $\beta_1$  on  $f'(\xi)$ .





**Figure 6:** Effect of  $\beta$  on  $g'(\xi)$ .

**Figure 9:** Effect of  $\beta_1$  on  $g'(\xi)$ .



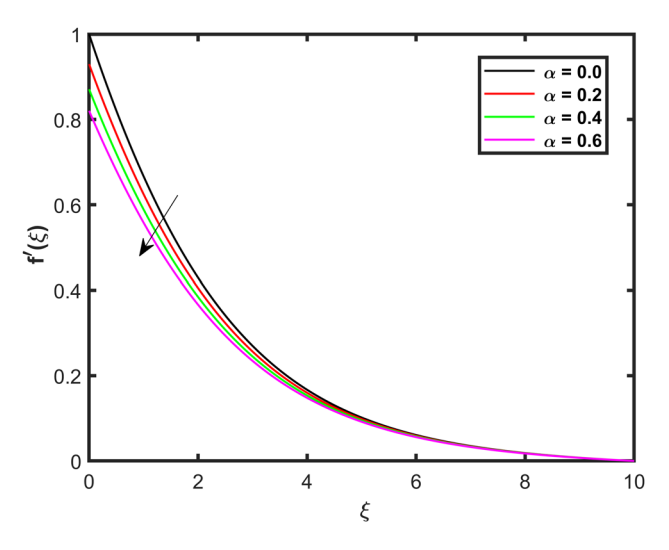


**Figure 7:** Effect of  $\beta$  on  $\theta(\xi)$ .

**Figure 10:** Effect of  $\alpha$  on  $f'(\xi)$ .

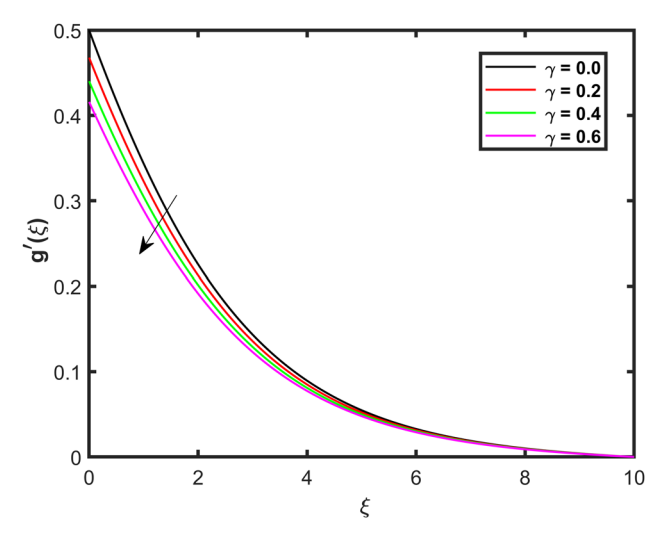


**Figure 11:** Effect of  $\gamma$  on  $g'(\xi)$ .

10

temperature  $(\theta(\xi))$  profiles via magnetic factor (M) for both slip and no-slip conditions. From Figures 2 and 3, we found that the higher values of M reduces both  $f'(\xi)$  and  $g''(\xi)$  for scenarios  $(\alpha=0.5)$  and  $(\alpha=0.0)$ . Physically, higher magnetic factor produces Lorentz force that opposes the fluid's motion which results in reducing the velocity profiles for both slip and no-slip conditions. However, a higher reduction in the velocity profiles is found for  $(\alpha=0.5)$  and  $(\alpha=0.0)$ . In the case of slip conditions, there exists a velocity gradient near the boundary which means that the particles of fluid are closer to the boundary and thus have slower velocity. In the case of magnetic field, the Lorentz force acts stronger on the particles of fluid near the boundary which shows that the velocity gradient is the greatest. Thus, high reductions in the velocity profiles are obtained. In the case

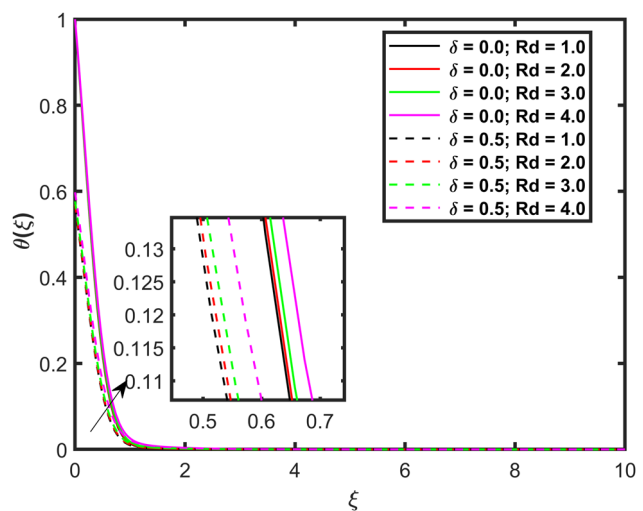


**Figure 13:** Effect of Rd on  $\theta(\xi)$ .

of no-slip conditions, the velocity of fluid particles at the boundary is zero which shows that there is no velocity gradient. Although the Lorentz force still acts on the fluid particles but the effect is smaller than in the case of slip conditions. Thus, in conclusion, the reductions in velocity profiles are higher in the case of slip conditions. From Figure 4, we have found that the higher values of M increases  $\theta(\xi)$  for both scenarios ( $\alpha=0.5$ ) and ( $\alpha=0.0$ ). The higher values of M increases  $\theta(\xi)$  more in the absence of slip condition (noslip) when compared to slip condition. Physically, the higher values of M increases the Lorentz force which significantly enhances the thermal distribution which results in higher thermal profile. In the case of no-slip condition, the particles of fluid that are in contact with the solid boundary have zero velocity relative to the surface, which leads to stronger

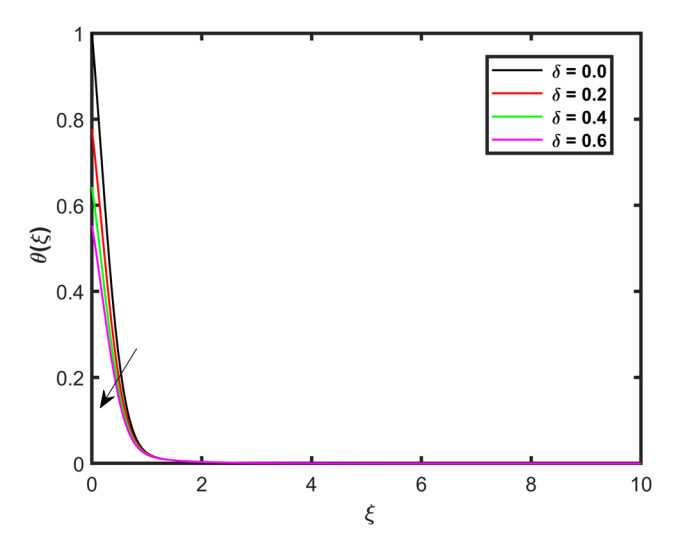


**Figure 12:** Effect of  $\delta$  on  $\theta(\xi)$ .

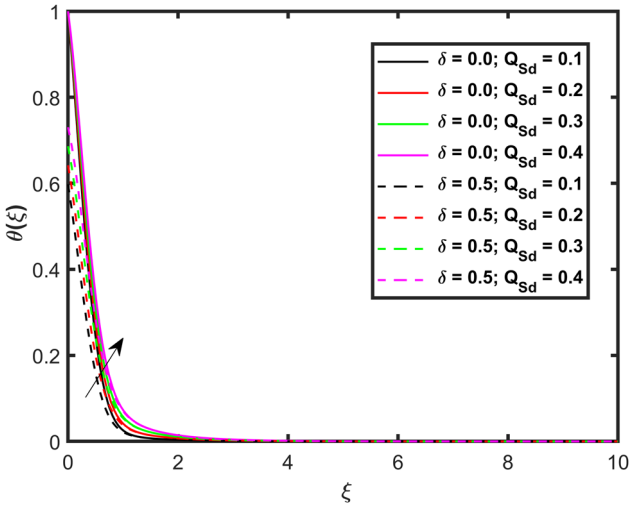


**Figure 14:** Effect of  $Q_{\rm Sd}$  on  $\theta(\xi)$ .

friction at the surface and as a result, there is an enhancement in the heat transfer. In the case of slip conditions, the heat transfer is enhanced with the higher magnetic factor, but this impact is still lesser than in the scenario ( $\alpha = 0.5$ ). Figures 5–7 portray the deviations in velocity  $(f'(\xi), g'(\xi))$ and temperature  $(\theta(\xi))$  profiles *via* Casson factor  $(\beta)$  for both slip and no-slip conditions. From Figures 5 and 6, we have found that higher values of  $\beta$  reduces both  $f'(\xi)$  and  $g'(\xi)$  for both the scenarios ( $\alpha = 0.5$ ) and ( $\alpha = 0.0$ ). The presence of the Casson factor shows the non-Newtonian behavior of the fluids with yield stress. In this case, the viscosity of the fluid is not constant but varies with the shear stress. As the Casson parameter increases, the resistance to the fluid flow becomes dominant, particularly at a lower shear rate, which results in reduction in the velocity profiles  $(f'(\xi), g'(\xi))$ . In contrast, as the Casson factor increases, the temperature distribution increases. As discussed in the above figures, higher Casson factor increases resistance to the fluid, as a result, the higher internal resistance is determined. Thus, due to a higher internal resistance in a flow system, the thermal distribution is enhanced. Looking at the slip and no-slip conditions, the higher velocity and temperature distributions are found for the case of no-slip conditions when compared to the slip conditions. Figures 8 and 9 display the deviations in velocity profiles  $(f'(\xi), g'(\xi))$  via ratio parameter ( $\beta_1$ ) for both slip and no-slip conditions. From Figures 8 and 9, we have found that the higher values of  $\beta_1$  reduces  $f'(\xi)$  and increases  $g'(\xi)$  for both scenarios  $(\alpha = 0.5)$  and  $(\alpha = 0.0)$ . The ratio factor shows the relation between the stretching constants of the primary (c) and secondary (b) velocities. From this relation, we see that the ratio factor is directly related to the constant of secondary velocity and inversely related to the constant of

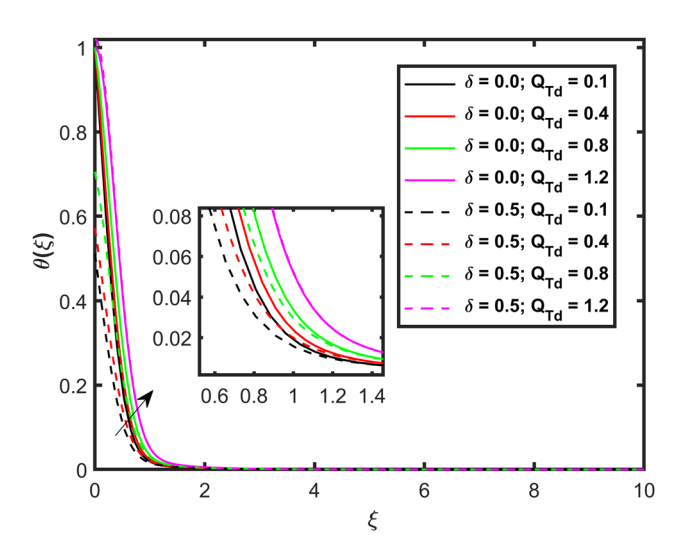


**Figure 15:** Effect of  $Q_{\rm Td}$  on  $\theta(\xi)$ .

primary velocity. By this relation, it is obvious that higher values of  $\beta_1$  reduces  $f'(\xi)$  while increases  $g'(\xi)$ . Looking at the scenarios ( $\alpha = 0.5$ ) and ( $\alpha = 0.0$ ), the higher velocity is found for the scenario ( $\alpha = 0.0$ ) when matched to the slip scenario. Figure 10 shows the variation in  $f'(\xi)$  via slip parameter ( $\delta$ ). From this Figure, we can see that the higher values of  $\alpha$  reduces  $f'(\xi)$ . In scenario ( $\alpha > 0$ ), there exists a velocity gradient near the boundary which means that the particles of fluid are closer to the boundary and thus have slower velocity. In the case of the no-slip condition ( $\alpha = 0$ ), the velocity of fluid particles at the boundary is zero which shows that there is no velocity gradient as shown in Figure 10. Figure 11 shows the variation in  $g'(\xi)$  via slip parameter (y). From this Figure, we can see that the higher values of yreduces  $g'(\xi)$ . In the case of slip condition ( $\gamma > 0$ ), there exists a velocity gradient near the boundary which means that the particles of fluid are closer to the boundary and thus have slower velocity. In the case of the no-slip condition (y = 0), the velocity of fluid particles at the boundary is zero which shows that there is no velocity gradient as shown in Figure 11. Figure 12 displays the variation in  $\theta(\xi)$  *via* slip parameter ( $\delta$ ). From this Figure, we can see that the higher values of  $\delta$  reduces  $\theta(\xi)$ . A temperature slip factor means that the fluid temperature at the solid surface is higher than the temperature of the solid surface itself. This indicates that there is a slip in temperature between the solid surface and fluid and as a result the heat transfer is enhanced. The higher heat transfer does not remain confined at the surface only but it also affects the thermal distribution within the porous medium. As a result, temperature slip enhances heat transmission close to the surface but loses effectiveness as one descends farther into the porous material. As a result, compared to a scenario without temperature slip, the temperature gradient across the medium is dropped overall as a result of the temperature slip parameter. Looking at the scenarios ( $\alpha = 0.5$ ) and ( $\alpha = 0.0$ ), the higher velocities and temperature profiles are found for scenario ( $\alpha = 0.0$ ) when compared to the scenario ( $\alpha$  = 0.5). Figure 13 shows the variations in temperature profile  $(\theta(\xi))$  *via* radiation factor (Rd) for both scenarios ( $\alpha = 0.5$ ) and ( $\alpha = 0.0$ ). In this Figure, we detected that high values of Rd increases  $\theta(\xi)$  for both scenarios ( $\alpha = 0.5$ ) and ( $\alpha = 0.0$ ). When Rd increases, there is maximum heat transmission occurring in a flow system. This means that additional heat is added to the flow system which consequently increases the thermal distribution. Looking at the slip and no-slip conditions, the higher temperature profile is found for the case of the no-slip condition when compared to the slip condition. Figures 14 and 15 show the variations in temperature profile  $(\theta(\xi))$ *via* space-dependent  $(Q_{Sd})$  and thermal-dependent  $(Q_{Td})$  heat sources for both scenarios ( $\alpha = 0.5$ ) and ( $\alpha = 0.0$ ). From these

Figures, we observed that higher values of  $Q_{\rm Sd}$  and  $Q_{\rm Td}$  increase  $\theta(\xi)$  for both scenarios ( $\alpha$  = 0.5) and ( $\alpha$  = 0.0). A heat source that relies on temperature for heat generation or absorption is known as a thermally dependent heat source. In general, the rate of heat generation or absorption increases with the temperature and vice versa. Because of the accelerated rate of heat creation in areas with thermally dependent heat sources, temperature tends to rise there. This may cause certain areas near the heat sources to get hotter than usual as shown in Figure 14. Similarly, increase in  $Q_{\rm Sd}$ , increases  $\theta(\xi)$  as shown in Figure 15. Looking at the scenarios ( $\alpha$  = 0.5) and ( $\alpha$  = 0.0), a higher temperature profile is found for scenarios ( $\alpha$  = 0.5) when compared to scenario ( $\alpha$  = 0.0).

## 6 Conclusion

In this analysis, the numerical investigation of a three-dimensional flow of SA-based nanofluid containing alumina nanoparticles (Al<sub>2</sub>O<sub>3</sub>) over a bi-directional extending sheet has been presented. The Cartesian coordinate system is chosen to solve the SA-based non-Newtonian Casson nanofluid flow. The variable Darcy porous media, magnetic field, thermal radiation, and thermal-dependent and space-dependent heat sources are applied to investigate heat transfer flow. The velocity slips and thermal slip conditions are also incorporated into the present model. Based on the present analysis, the following key points are obtained:

- Higher magnetic parameter increases thermal distribution, skin friction, and heat transfer rate and reduces the velocity profiles along both directions.
- The Casson parameter reduces the skin frictions, heat transfer rate, and velocity profiles along both directions while increasing thermal distribution.
- The velocity ratio factor increases the skin friction and secondary velocity distribution while reducing the primary velocity distribution.
- The primary velocity slip, secondary velocity slip, and thermal slip factors reduce the temperature and both the velocity distributions.
- The space-dependent and thermal-dependent heat source factors increase the heat transfer rates and thermal distribution.
- Higher velocities and temperature distributions of the three-dimensional flow of a SA-based nanofluid containing alumina nanoparticles are found for the case of the no-slip condition when compared to the slip condition.
- It is concluded from the observed results presented in Tables 4 and 5 that the percentage increase is higher for the no-slip conditions compared to the slip conditions.

## 7 Future recommendations

In the future, the present work can be extended by considering viscous dissipation, Joule heating, heat sources, and stretching/shrinking, as well as thermal and mass flux conditions. Furthermore, different types of metallic and non-metallic nanoparticles, along with various base fluids over different physical surfaces, can be considered to investigate the flow behavior.

**Acknowledgments:** The author extends his appreciation to the Deputyship for Research & Innovation, Ministry of Education in Saudi Arabia for funding this research work through the project number INST225.

**Funding information:** This work was funded by the Deputyship for Research & Innovation, Ministry of Education in Saudi Arabia through the project number INST225.

**Author contributions:** The author has accepted responsibility for the entire content of this manuscript and approved its submission.

**Conflict of interest:** The author states no conflict of interest.

**Data availability statement:** The datasets generated and/ or analysed during the current study are available from the corresponding author on reasonable request.

#### References

- [1] Choi SUS, Eastman JA. Enhancing thermal conductivity of fluids with nanoparticles. 1995 Int Mech Eng Congr Exhib. San Fr CA, United States: 12–17 Nov 1995.
- [2] Hussain SM, Jamshed W, Safdar R, Shahzad F, Mohd Nasir NAA, Ullah I. Chemical reaction and thermal characteristics of Maxwell nanofluid flow-through solar collector as a potential solar energy cooling application: A modified Buongiorno's model. Energy Env. 2022;0958305X221088113.
- [3] Shah Z, Khan A, Khan W, Alam MK, Islam S, Kumam P, et al. Micropolar gold blood nanofluid flow and radiative heat transfer between permeable channels. Comput Methods Prog Biomed. 2020;186:105197.
- [4] Varun Kumar RS, Gunderi Dhananjaya P, Naveen Kumar R, Punith Gowda RJ, Prasannakumara BC. Modeling and theoretical investigation on Casson nanofluid flow over a curved stretching surface with the influence of magnetic field and chemical reaction. Int J Comput Methods Eng Sci Mech. 2022;23:12–9.
- [5] Acharya N, Mabood F, Shahzad SA, Badruddin IA. Hydrothermal variations of radiative nanofluid flow by the influence of nanoparticles diameter and nanolayer. Int Commun Heat Mass Transf. 2022;130:105781.

- [6] Gherieb S, Kezzar M, Ayub A, Sari MR, Khan U, Muhammad T, et al. Insight into the dynamics of slip and radiative effect on magnetohydrodynamic flow of hybrid ferroparticles over a porous deformable sheet. ZAMM-Journal Appl Math Mech Für Angew Math Und Mech. 2024;e202300729.
- [7] Lone SA, Khan A, Gul T, Mukhtar S, Alghamdi W, Ali I. Entropy generation for stagnation point dissipative hybrid nanofluid flow on a Riga plate with the influence of nonlinear convection using neural network approach. Colloid Polym Sci. 2024;1–26.
- [8] Asghar A, Ying TY, Zaimi WMKAW. Two-dimensional mixed convection and radiative Al<sub>2</sub>O<sub>3</sub>-Cu/H<sub>2</sub>O hybrid nanofluid flow over a vertical exponentially shrinking sheet with partial slip conditions. CFD Lett. 2022;14:22–38.
- [9] Bhatti MM, Öztop HF, Ellahi R. Study of the magnetized hybrid nanofluid flow through a flat elastic surface with applications in solar energy. Mater (Basel). 2022;15:7507.
- [10] Asghar A, Lund LA, Shah Z, Vrinceanu N, Deebani W, Shutaywi M. Effect of thermal radiation on three-dimensional magnetized rotating flow of a hybrid nanofluid. Nanomaterials. 2022;12:1566.
- [11] Asghar A, Vrinceanu N, Ying TY, Lund LA, Shah Z, Tirth V. Dual solutions of convective rotating flow of three-dimensional hybrid nanofluid across the linear stretching/shrinking sheet. Alex Eng J. 2023;75:297–312.
- [12] Waqas H, Farooq U, Liu D, Abid M, Imran M, Muhammad T. Heat transfer analysis of hybrid nanofluid flow with thermal radiation through a stretching sheet: A comparative study. Int Commun Heat Mass Transf. 2022;138:106303. doi: 10.1016/J. ICHEATMASSTRANSFER.2022.106303.
- [13] Al-Kouz W, Owhaib W, Ayub A, Souayeh B, Hader M, Homod RZ, et al. Thermal proficiency of magnetized and radiative crossternary hybrid nanofluid flow induced by a vertical cylinder. Open Phys. 2024;22:20230197.
- [14] Ray PK, Bouvier D, Papageorgiou DT. Flow of shear-thinning liquids in channels with superhydrophobic surfaces. J Nonnewton Fluid Mech. 2023;319:105091.
- [15] Vishal G, Garg A, Sarkar J, Pattanayek SK. The channel flow of a real shear thickening fluid using the lattice Boltzmann simulation and the theoretical model. 2023.
- [16] Hosseinzadeh K, Mardani MR, Paikar M, Hasibi A, Tavangar T, Nimafar M, et al. Investigation of second grade viscoelastic non-Newtonian nanofluid flow on the curve stretching surface in presence of MHD. Results Eng. 2023;17:100838.
- [17] Asghar Z, Khan MWS, Pasha AA, Rahman MM, Sankaralingam L, Alam MI. On non-Newtonian fluid flow generated via complex metachronal waves of cilia with magnetic, hall, and porous effects. Phys Fluids. 2023;35:093601.
- [18] Rahmani H, Larachi F, Taghavi SM. Modeling of shear flows over superhydrophobic surfaces: from Newtonian to non-Newtonian fluids. ACS Eng Au. 2024;4(2):166–92.
- [19] Madhu J, Baili J, Kumar RN, Prasannakumara BC, Gowda RJP. Multilayer neural networks for studying three-dimensional flow of non-Newtonian fluid flow with the impact of magnetic dipole and gyrotactic microorganisms. Phys Scr. 2023;98:115228.
- [20] Nazeer M, Alqarni MZ, Hussain F, Saleem S. Computational analysis of multiphase flow of non-Newtonian fluid through inclined channel: heat transfer analysis with perturbation method. Comput Part Mech. 2023;1–11.
- [21] Biswal MM, Swain K, Dash GC, Ojha K. Study of radiative magnetonon-Newtonian fluid flow over a nonlinearly elongating sheet with

- Soret and Dufour effects. Numer Heat Transf Part A Appl. 2023:83:331–42.
- [22] Zaman SU, Nauman Aslam M, Hussain A. Chemically reactive MHD fluid flow along with thermophoresis and Brownian effects. Adv Mech Eng. 2023;15:16878132231193326.
- [23] Ahmad S, Ali K, Castellanos HG, Aryanfar Y, Rashid FL, Hendy AS, et al. Complex dynamics of induced vortex formation and thermal-fluid coupling in tri-hybrid nanofluid under localized magnetic field: a novel study. Sci Rep. 2023;13:21140.
- [24] Ali K, Ahmad S, Ahmad S, Tayebi T. Impact of magnetic field localization on the vortex generation in hybrid nanofluid flow. J Therm Anal Calorim. 2023;1–18.
- [25] Wang Y, Cheng K, Xu J, Jing W, Huang H, Qin J. A rapid performance prediction method for Two-Phase liquid metal MHD generators based on Quasi-One-Dimensional model. Therm Sci Eng Prog. 2024;47:102258.
- [26] Zhu S, Yu G, Jiang C, Wang T, Zhang L, Wu Z, et al. A novel ther-moacoustically-driven liquid metal magnetohydrodynamic generator for future space power applications. Energy Convers Manag. 2022;258:115503.
- [27] Boujelbene M, Rehman S, Alqahtani S, Alshehery S, Eldin SM. Thermal transport and magnetohydrodynamics flow of generalized Newtonian nanofluid with inherent irreversibility between conduit with slip at the walls. Eng Appl Comput Fluid Mech. 2023;17:2182364.
- [28] Tarakaramu N, Satya Narayana PV, Sivakumar N, Harish Babu D, Bhagya Lakshmi K. Convective conditions on 3D Magnetohydrodynamic (MHD) non-Newtonian nanofluid flow with nonlinear thermal radiation and heat absorption: A numerical analysis. J Nanofluids. 2023;12:448–57.
- [29] Mirzaei A, Jalili P, Afifi MD, Jalili B, Ganji DD. Convection heat transfer of MHD fluid flow in the circular cavity with various obstacles: Finite element approach. Int J Thermofluids. 2023:20:100522.
- [30] Ayub A, Asjad MI, Al-Malki MAS, Khan S, Eldin SM, Abd El-Rahman M. Scrutiny of nanoscale heat transport with ion-slip and Hall current on ternary MHD cross nanofluid over heated rotating geometry. Case Stud. Therm Eng. 2024;53:103833.
- [31] Botmart T, Ayub A, Sabir Z, Weera W, Sadat R, Ali MR. Infinite shear rate aspect of the cross-nanofluid over a cylindrical channel with activation energy and inclined magnetic dipole effects. Waves Random Complex Media. 2022;1–21.
- [32] Lund LA, Asghar A, Rasool G, Yashkun U. Magnetized Casson Sahybrid nanofluid flow over a permeable moving surface with thermal radiation and Joule heating effect. Case Stud Therm Eng. 2023;50:103510.
- [33] Santos-Moreno M, Valencia-Negrete CV, Fernandez-Anaya G. Conformable derivatives in viscous flow describing fluid through porous medium with variable permeability. Fractals. 2022;30:2250178.
- [34] Cherifa B, Mohamed B, Abderrahim M, Fatima-Zohra K. Unsteady natural convection in a porous square cavity saturated by nanofluid using buongiorno model: variable permeability effect on homogeneous porous medium. CFD Lett. 2022;14:42–61.
- [35] Trilok G, Kumar KK, Gnanasekaran N, Mobedi M. Numerical assessment of thermal characteristics of metal foams of orderly varied pore density and porosity under different convection regimes. Int J Therm Sci. 2022;172:107288.
- [36] Zhuang Y, Liu Z, Xu W. Effects of gradient porous metal foam on the melting performance and energy storage of composite phase

- change materials subjected to an internal heater: A numerical study and PIV experimental validation. Int J Heat Mass Transf. 2022;183:122081.
- [37] Reddy YD, Goud BS, Nisar KS, Alshahrani B, Mahmoud M, Park C. Heat absorption/generation effect on MHD heat transfer fluid flow along a stretching cylinder with a porous medium. Alex Eng J. 2023;64:659–66.
- [38] Hussain M, Sheremet M. Convection analysis of the radiative nanofluid flow through porous media over a stretching surface with inclined magnetic field. Int Commun Heat Mass Transf. 2023:140:106559.
- [39] Khan A, Alyami MA, Alghamdi W, Alqarni MM, Yassen MF, Tag Eldin E. Thermal examination for the micropolar gold ± blood nanofluid flow through a permeable channel subject to gyrotactic microorganisms. Future. 2022;1:1.
- [40] Gorai D, Duari PR, Das K. Influence of variable characteristic of the porous medium on unsteady nanofluid flow with melting heat transference. Numer Heat Transf Part A Appl. 2024;85:702–18.
- [41] Yu D, Wang R. An optimal investigation of convective fluid flow suspended by carbon nanotubes and thermal radiation impact. Mathematics. 2022;10:1542.
- [42] Sharma BK, Kumar A, Gandhi R, Bhatti MM, Mishra NK. Entropy generation and thermal radiation analysis of EMHD Jeffrey nanofluid flow: applications in solar energy. Nanomaterials. 2023;13:1–23. doi: 10.3390/nano13030544.
- [43] Goud BS, Reddy YD, ADNAN. Numerical investigation of the dynamics of magnetized Casson fluid flow over a permeable wedge subject to dissipation and thermal radiations. Surf Rev Lett. 2023;2450054.
- [44] Kodi R, Ravuri MR, Veeranna V, Khan MI, Abdullaev S, Tamam N. Hall current and thermal radiation effects of 3D rotating hybrid nanofluid reactive flow via stretched plate with internal heat absorption. Results Phys. 2023;53:106915.
- [45] Saraswathy M, Prakash D, Durgaprasad P. MHD micropolar fluid in a porous channel provoked by viscous dissipation and non-linear thermal radiation: an analytical approach. Mathematics. 2022;11:183.
- [46] Tarakaramu N, Reddappa B, Radha G, Abduvalieva D, Sivakumar N, Awwad FA, et al. Thermal radiation and heat generation on threedimensional Casson fluid motion via porous stretching surface with variable thermal conductivity. Open Phys. 2023;21:20230137.
- [47] Guedri K, Mahmood Z, Fadhl BM, Makhdoum BM, Eldin SM, Khan U. Mathematical analysis of nonlinear thermal radiation and nanoparticle aggregation on unsteady MHD flow of micropolar nanofluid over shrinking sheet. Heliyon. 2023;9.
- [48] Farooq U, Jan A, Hussain M. Impact of thermal radiations, heat generation/absorption and porosity on MHD nanofluid flow towards an inclined stretching surface: Non-similar analysis. ZAMM – J Appl Math Mech/Zeitschrift Für Angew Math Und Mech. 2023;e202300306. doi: 10.1002/ZAMM.202300306.
- [49] Darvesh A, Altamirano GC, Salas S AH, Sánchez Chero M, Carrión Barco G, Bringas Salvador JL, et al. Infinite shear rate viscosity

- model of cross fluid flow containing nanoparticles and motile gyrotactic microorganisms over 3-D cylinder. J Nanofluids. 2023;12:930–41.
- [50] Asghar A, Ying TY, Zaimi K. Two-dimensional magnetized mixed convection hybrid nanofluid over a vertical exponentially shrinking sheet by thermal radiation, Joule heating, velocity and thermal slip conditions. J Adv Res Fluid Mech Therm Sci. 2022;95:159–79. doi: 10. 37934/ARFMTS.95.2.159179.
- [51] Nithiarasu P, Seetharamu KN, Sundararajan T. Natural convective heat transfer in a fluid saturated variable porosity medium. Int J Heat Mass Transf. 1997;40:3955–67.
- [52] Tlau L, Ontela S. Entropy analysis of hybrid nanofluid flow in a porous medium with variable permeability considering isothermal/ isoflux conditions. Chin J Phys. 2022;80:239–52.
- [53] Issa C, Chamkha AJ, Khanafer K. Natural convection from an inclined plate embedded in a variable porosity porous medium due to solar radiation. Int J Therm Sci. 2002;41(1):73–81.
- [54] Nakamura M, Sawada T. Numerical study on the flow of a non-Newtonian fluid through an axisymmetric stenosis. J Biomech Eng. 1988;110:137–43. doi: 10.1115/1.3108418.
- [55] Dawar A, Wakif A, Saeed A, Shah Z, Muhammad T, Kumam P. Significance of Lorentz forces on Jeffrey nanofluid flows over a convectively heated flat surface featured by multiple velocity slips and dual stretching constraint: a homotopy analysis approach. J Comput Des Eng. 2022;9:564–82.
- [56] Waqas H, Farooq U, Alqarni MS, Muhammad T. Numerical investigation for 3D bioconvection flow of Carreau nanofluid with heat source/sink and motile microorganisms. Alex Eng J. 2022;61:2366–75.
- [57] Dawar A, Islam S, Shah Z, Mahmuod SR. A passive control of Casson hybrid nanofluid flow over a curved surface with alumina and copper nanomaterials: A study on sodium alginate-based fluid. J Mol Liq. 2023;382:122018.
- [58] Dawar A, Thumma T, Islam S, Shah Z. Optimization of response function on hydromagnetic buoyancy-driven rotating flow considering particle diameter and interfacial layer effects: Homotopy and sensitivity analysis. Int Commun Heat Mass Transf. 2023;144:106770. doi: 10.1016/J.ICHEATMASSTRANSFER.2023. 106770.
- [59] Dawar A, Islam S, Shah Z. A comparative analysis of the performance of magnetised copper-copper oxide/water and copper-copper oxide/kerosene oil hybrid nanofluids flowing through an extending surface with velocity slips and thermal convective conditions. Int J Ambient Energy. 2022;43:7330–48. doi: 10.1080/01430750.2022.2063387.
- [60] Khan WA, Pop I. Boundary-layer flow of a nanofluid past a stretching sheet. Int J Heat Mass Transf. 2010;53:2477–83.
- [61] Reddy Gorla RS, Sidawi I. Free convection on a vertical stretching surface with suction and blowing. Appl Sci Res. 1994:52:247–57.
- [62] Al-Kouz W, Owhaib W. Numerical analysis of Casson nanofluid three-dimensional flow over a rotating frame exposed to a prescribed heat flux with viscous heating. Sci Rep. 2022;12:1–17.